Direct numerical simulations of three-dimensional flows past obstacles with a vortex penalization method

Chloé Mimeau, Georges-Henri Cottet, Iraj Mortazavi

Direct numerical simulations of three-dimensional flows past obstacles with a vortex penalization method

C. Mimeau[a,1], G.-H. Cottet[b,2], I. Mortazavi[c,2,*]

[a] *Conservatoire National des Arts et Métiers, Laboratoire DynFluid, 151, boulevard de l'Hôpital, 75013 Paris, FRANCE*
[b] *Univ. Grenoble-Alpes, LJK, 51 rue des Mathématiques, F-38041 Grenoble FRANCE*
[c] *EA-7340-M2N-Modélisation, Mathématique et Numérique, Case 2D5000 Conservatoire National des Arts et Métiers, 292 Rue St Martin, 75003 Paris FRANCE*

Abstract

A vortex method with penalization is proposed in order to simulate three-dimensional incompressible bluff body flows. This approach combines the robustness of vortex methods and the flexibility of penalization methods to impose boundary conditions on the obstacle. Far field boundary conditions are handled in a FFT-based Poisson solver. A validation of the proposed numerical method is carried out in the context of flow past a sphere and further simulations are performed in the more challenging case of flow past a hemisphere.

Keywords: flow past a sphere, flow past a hemisphere, vortex methods, particle methods, penalization method, semi-Lagrangian methods.

1. Introduction

Vortex methods are Lagrangian methods consisting in discretizing the vorticity on particles which move with the flow and carry local vorticity values. They approximate the vorticity formulation of the Navier-Stokes equations (Vorticity Transport Equation) focusing the computational task on the vortical zones, thus allowing to reduce the simulation time. They

*Corresponding author
Email address: iraj.mortazavi@cnam.fr (I. Mortazavi)
[1]Present address
[2]Permanent address

are ideal for vortex-dominated flow simulations, like flows past bluff-bodies, airfoils, propellers, turbine profiles as well as complex internal configurations, thanks to a lower numerical diffusion and the dynamic adaptivity of the particles to the support of the vorticity. Moreover, continuity and far-field boundary conditions are satisfied by construction.

Vortex methods have been widely used to study wakes and more generally advection dominated flows and several works have provided these methods a solid mathematical framework to understand their convergence[1].

For external flows, vortex methods often rely on the use of Fast Multipole Methods (FMM). This technique, introduced by [2], allows to reduce the algorithm complexity of the computation of the velocity of the vortex elements from $\mathcal{O}(N^2)$, obtained with a classical resolution of the Biot-Savart law, to $\mathcal{O}(N \log(N))$. This has been widely used in the context of vortex methods [3, 4, 5, 6, 7]. Alternatively, vortex methods can rely on grid-based Poisson solver to compute velocity fields [8]. In that case vorticity values have to be interpolated to the grid and velocity values have to be interpolated back to particles. In particular [9] indicates comparisons of CPU times between FMM and methods based on Poisson solvers which indicate that, except if the support of vorticity has very small dimension compared to the computational box, Poisson-based vortex methods are more economical in 3D than FMM-based vortex methods, by several order of magnitudes. However [7] shows that, when implemented on GPU with very large numbers of particles, FMM-based methods can close the gap with vortex methods based on Poisson solvers.

Vortex methods, and more generally particle methods, also face accuracy issues related to particle distortions. One popular method to handle this issue is to remesh frequently - in general at each time-step - particles on regular grids. This method was used in [3] to obtain reference results for flows past a 2D circular cylinder. With this technique, particle methods become semi-Lagrangian methods and their accuracy can be rigorously analyzed in terms of the interpolation kernels used to remesh particles [10] under stability conditions on the time-step which do not rely on the inter-particle spacing. In remeshed vortex methods, vorticity grid values obtained after particle remeshing can be readily used to obtain the velocity through a grid-based Poisson solver. Alternative methods allow to adapt velocity and diffusion kernels to the distribution of particles [11, 12] or to adapt the particle distribution to the boundaries [13] (see also [1] for earlier references on this issue) . However, to our knowledge, this type of methods has not been

implemented yet in 3D flows.

A third issue faced by vortex methods, and more generally by all methods based on the vorticity formulation of the Navier-Stokes equations, is related to boundary conditions. The no-slip condition can be turned into a vorticity flux boundary condition that can be handled together with the vorticity diffusion by integral equations [14, 15]. This method has been used with success in a number of two and three-dimensional simulations using vortex particles [3, 4, 9]. These simulations use body-fitted particle distributions. Alternative methods, primarily defined and used in the context of grid-based Eulerian methods [16, 17], consist in viewing obstacles as immersed boundaries which appear as a forcing term in the Navier-Stokes equations. Immersed boundary methods can easily be implemented on a non-conforming grid or particle distribution, albeit at the expense of a lower accuracy near the boundary. The Brinkman penalization method is a particular case of immersed boundary methods where the velocity is penalized inside the obstacle. Penalization methods can be interpreted as originally formulated in velocity-pressure formulation and can be extended to vorticity formulations [18] and to vortex methods [19].

Vortex methods using a penalization method to enforce the no-slip condition have been developed and used in the context of fluid-structure interaction problems [19, 20]. In [21] the algorithmic simplicity of the penalization method was utilized to enable an efficient GPU implementation of the method for 2D bluff-body flows. In [22, 23] the method was in particular used to model flows around turbines or to optimize porous layers for passive control to reduce drag behind a semi-circular cylinder.

In the present method we study flows past a sphere and an hemisphere and we specifically focus on two new aspects of the method which significantly reduce the computational cost of the method: we propose a simple method relying on FFT-based Poisson solvers to approximate the far field boundary conditions and we extend the directional remeshing technique introduced in [24, 10] to the three-dimensional Navier-Stokes equation.

This paper is organized as follows. In the first three sections we recall the governing equations, we indicate how the body forces are computed in such a model and we detail our treatment of the far-field boundary conditions. In section 5 we detail the algorithm and the numerical schemes to discretize the problem. Section 6 is devoted to the numerical results. We perform a validation and a convergence study of the proposed method for three-dimensional flows past a sphere. We then present similar investigations in

the context of flows around a hemisphere. In this section we also discuss the computational cost and parallel scalability of the method. Finally, some conclusions and perspectives related to the present work are outlined in the last section.

2. Governing equations

This study is based on the vorticity formulation of the incompressible Navier-Stokes equations in a domain D, which read:

$$\frac{\partial \boldsymbol{\omega}}{\partial t} + (\mathbf{u} \cdot \nabla)\boldsymbol{\omega} - (\boldsymbol{\omega} \cdot \nabla)\mathbf{u} = \frac{1}{Re}\Delta\boldsymbol{\omega} \quad \text{in } D. \tag{1}$$

In this equation $\boldsymbol{\omega}$, $\mathbf{u}$ and Re respectively denote the vorticity, the velocity and the Reynolds number. This equation has to be coupled to the system giving the velocity in terms of the vorticity. Using the incompressibility condition, the velocity may be directly linked to the vorticity through the following Poisson equation:

$$\Delta\mathbf{u} = -\nabla \times \boldsymbol{\omega}. \tag{2}$$

The system (1)-(2) has to be complemented by appropriate boundary conditions, both at solid boundaries and, if necessary, at artificial boundaries. This latter issue will be addressed in detail in section 4. The modeling of incompressible flow around an obstacle is realized in this work using the Brinkman penalization method [25, 16]. This technique relies on the simple following idea: the fluid in which the flow evolves is assumed to be a porous medium of infinite permeability while, on the other hand, the solid obstacles immersed in the fluid are considered as media with zero permeability. A flow evolving in such media may be modeled by the Brinkman-Navier-Stokes equations, which stands for the whole domain and which contains an additional term in the Navier-Stokes equations, acting as a forcing term. The latter, called the penalization term, directly comes from the Darcy equations that govern flows in porous media. In this work, the penalization term is expressed using vorticity formulation. One therefore obtains the non-dimensional penalized Vorticity-Transport-Equations (or Brinkman-Navier-Stokes equations), originally proposed by [18]:

$$\frac{\partial \boldsymbol{\omega}}{\partial t} + (\mathbf{u} \cdot \nabla)\boldsymbol{\omega} - (\boldsymbol{\omega} \cdot \nabla)\mathbf{u} = \nabla \times \Big(\lambda\ \chi_b(\mathbf{u}_b - \mathbf{u})\Big) + \frac{1}{Re}\Delta\boldsymbol{\omega} \quad \text{in } D, \tag{3}$$

$$\Delta\mathbf{u} = -\nabla \times \boldsymbol{\omega} \quad \text{in } D, \tag{4}$$

where χ_b denotes the characteristic function that yields 0 in the fluid and 1 in the solid body, $\mathbf{u}_b$ indicates the rigid body velocity and $\lambda = \mu\Phi H/\rho k\mathbf{u}_\infty$ is the non-dimensional penalization parameter, with k the intrinsic permeability, μ the viscosity, Φ the porosity of the porous material, H the height of the obstacle, ρ the fluid density and $\mathbf{u}_\infty$ the main uniform fluid flow velocity.

The main advantage of this method is that it needs neither the mesh to fit the boundaries nor to specify no-slip boundary conditions. Moreover, the penalized Vorticity-Transport-Equation (3) appears to be very convenient to model the flow in the whole domain thanks to the dimensionless penalization factor λ, whose value allows to distinguish between the different materials. In this study we set $H = \rho = u_\infty = 1$ and we recall that the porosity Φ is close to 1 as imposed by the Brinkman equation [26]. Therefore λ essentially depends, in the inverse proportion, on the intrinsic permeability k of the medium. Varying the value of λ thus directly defines the different media. Indeed, in the fluid, the intrinsic permeability coefficient k goes to infinity, thus the fluid can be considered numerically as a porous media with a very high permeability. We set $\lambda = 0$ in this region. As a consequence, the penalization term vanishes in equation (3), and we naturally recover the dimensionless Vorticity Transport Equation (1). On the contrary, the solid has a permeability coefficient k close to zero, it can be consequently modeled by fixing the penalization parameter λ to a very high value. In this study λ is set to 10^8 in the solid. It was proved in [16] that solving equation (3) with such a value of λ was equivalent to solve Darcy's law in the solid. As a conclusion, at a given flow regime, the variation of λ corresponds to the variation of k and specifies the intrinsic porous material permeability. Figure 1 gives a schematic representation of the overall physical representation and the associated numerical settings. The physical description (left picture) involves the physical quantities H, $\mathbf{u}_\infty$, Φ, k and $\nu = \mu/\rho$. The associated numerical setting (right picture) involves the characteristic function χ_b enabling to geometrically define the solid body as well as the penalization term $\lambda = \nu\Phi H/k\mathbf{u}_\infty$ obtained from the adimensionalization of the penalized Navier-Stokes equations and allowing to numerically specify the permeability of the considered medium. For further details about the derivation of the penalized Vorticity-Transport-Equations from the Brinkman equation, the reader is referred to the work [23].

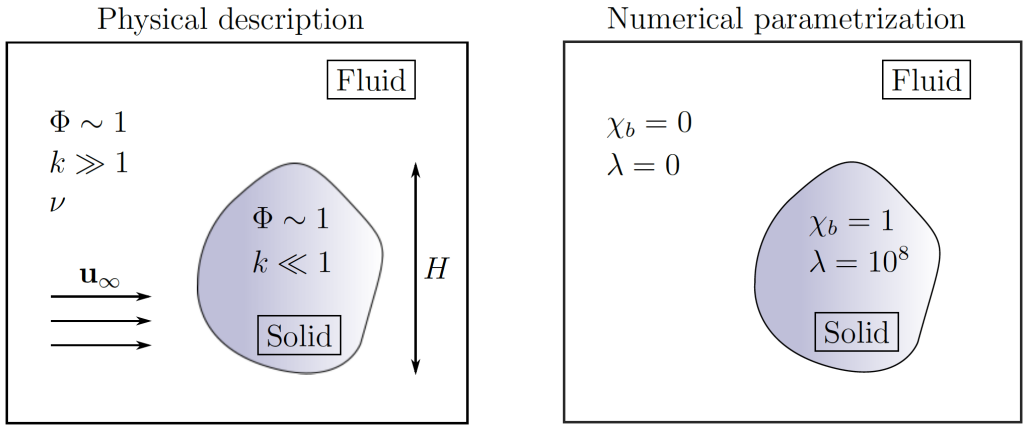

Figure 1: Schematic representation of the physical description (left) and its numerical parametrization (right) for flow past a solid body using the penalization method framework.

3. Forces evaluation

The accurate computation of the unsteady aerodynamic force exerted by the fluid on an immersed body is important in the framework of this study. Indeed, the force provides a reliable diagnostic to validate the ability of the proposed method to model the problem correctly. The method adopted in this work to compute the aerodynamic force in three-dimensions is the numerical approach introduced by [27] under the name of *change of momentum*. It is based on the fact that the time dependent force exerted by a fluid on a body B of constant mass is directly proportional to the body acceleration. For unit density one has:

$$F = -\frac{d}{dt}\int_B \mathbf{u}\, d\mathbf{x}. \tag{5}$$

If we think in terms of numerical iterative process, we can consider that, at each time step, the fluid is allowed to enter inside the rigid body before the penalization term enforces the velocity $\mathbf{u}$ to be equal to $\mathbf{u}_\lambda$ inside the body. Therefore, the obstacle experiences the following change of momentum $\Delta\mathbf{q}$:

$$\Delta\mathbf{q} = \int_B (\mathbf{u} - \mathbf{u}_\lambda)\, d\mathbf{x}, \tag{6}$$

and the force is finally obtained by the formula:

$$F = \frac{d}{dt} \int_B (\mathbf{u} - \mathbf{u}_\lambda) \, d\mathbf{x}. \tag{7}$$

The drag and lift coefficients are then defined by:

$$C_D = \frac{F_x}{\mathcal{Q} \times \mathcal{A}}, \qquad C_L = \frac{F_y}{\mathcal{Q} \times \mathcal{A}}, \qquad C_S = \frac{F_z}{\mathcal{Q} \times \mathcal{A}}, \tag{8}$$

where the lift coefficient is decomposed into C_L (vertical lift) and C_S (side lift), $\mathcal{Q} = \frac{1}{2}\rho u_\infty^2$ denotes the dynamic pressure and $\mathcal{A}$ is the reference area.

As this force calculation method is inherently based on the penalization technique, that is to say on the continuous velocity enforcement inside the body, it appears as a natural choice in the framework of the present numerical method. However, it may show some limits when high Reynolds numbers are considered, due to the grid refinements needed to accurately take into account the obstacle boundaries. In this case, other formulations may be used, like for instance the one proposed by [28] where the forces are evaluated on a control volume that includes the solid body.

4. Far-field boundary conditions

In the present study we consider flows past obstacles in a domain with a prescribed inlet normal velocity and periodic boundary conditions in the transverse directions. To obtain optimal computational efficiency we will use periodic boundary conditions in all directions, which will allow to rely on simple FFT to obtain the velocity from the vorticity. This however requires appropriate corrections to account for the inflow and outflow boundary conditions.

4.1. Solenoidal eddies absorption

A first consequence of periodic boundary conditions is the emergence, in the upstream region, of eddies coming periodically from the outlet (we suppose in this study that the domain has a sufficient size in the y and z directions so that the wake do not reach the concerned boundaries). In order to discard these arising vortices, one needs to apply a specific treatment on the vorticity field. This treatment consists in an absorption, in the flow direction, of the vorticity within a band located at the outlet of the domain.

More precisely we proceed as follows. Given a periodic vorticity field $\boldsymbol{\omega}_{\text{periodic}}$ and its associated velocity field $\mathbf{u}_{\text{periodic}}$ we first define:

$$\tilde{\mathbf{u}} = f(x)\ \mathbf{u}_{\text{periodic}} + (1 - f(x))\ \mathbf{u}_{\infty}, \tag{9}$$

where f is the following one-dimensional smoothing function defined in the flow direction [29]:

$$f(x) = \begin{cases} 1 & \text{if } \ x < x_b \\ \dfrac{\tanh(\alpha(x - x_c)) - \tanh(\alpha(x_e - x_c))}{\tanh(\alpha(x_b - x_c)) - \tanh(\alpha(x_e - x_c))} & \text{if } \ x_b \leq x \leq x_e \\ 0 & \text{if } \ x > x_e. \end{cases} \tag{10}$$

In the above expression x_b, x_c and x_e respectively refer to the beginning, the center and the end of the absorption band at the outlet (see Figure 2). The parameter α allows to adjust the steepness of the absorption function f.

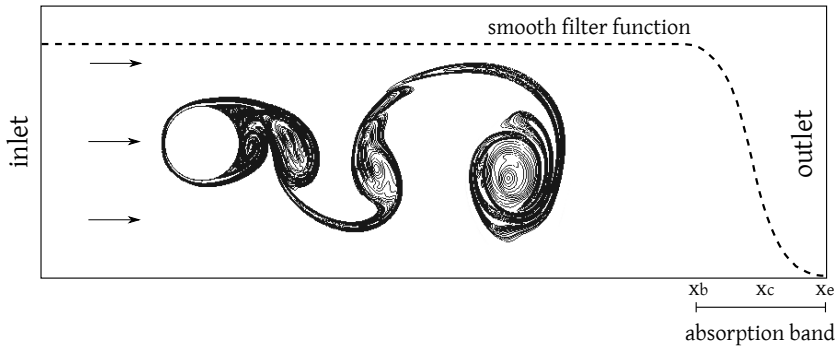

Figure 2: Schematic representation of the smooth vorticity absorption performed at the outlet.

One then obtains a corrected vorticity field:

$$\tilde{\boldsymbol{\omega}} = \nabla \times \tilde{\mathbf{u}} \tag{11}$$

$$= f(x)\ \boldsymbol{\omega}_{\text{periodic}} + [\nabla f(x) \times \mathbf{u}_{\text{periodic}}] + \nabla[1 - f(x)] \times \mathbf{u}_{\infty} \tag{12}$$

$$= \begin{pmatrix} \omega_x\ f(x) \\ \omega_y\ f(x) \\ \omega_z\ f(x) \end{pmatrix} + \begin{pmatrix} 0 \\ -f'(x)u_z \\ f'(x)u_y \end{pmatrix} + \begin{pmatrix} 0 \\ f'(x)u_{z\infty} \\ -f'(x)u_{y\infty} \end{pmatrix}. \tag{13}$$

Note that the above absorption guarantees the solenoidal condition div $\boldsymbol{\omega} = 0$, a property which would not be satisfied if the absorption mechanism (9) was applied directly to the vorticity.

4.2. Velocity correction

Our choice of periodic boundary conditions in the Poisson solver to compute the velocity from the vorticity requires to adjust the correct flux through the computational box. Moreover, periodic boundary conditions also imply a zero circulation, i.e. $\int_D \boldsymbol{\omega} = 0$. This condition is not satisfied as soon as eddies leave the computational box and a correction is needed to account for the non-zero circulation. In the sequel x denotes the direction along which the inlet velocity is prescribed and y and z the transverse directions where periodic boundary conditions are assumed.

To derive the correction enforced on the velocity calculations we introduce the following notation:

$$\mathbf{u} = \widetilde{\mathbf{u}} + \overline{\mathbf{u}}. \tag{14}$$

In this relation, $\widetilde{\mathbf{u}}$ denotes the output velocity field obtained from the FFT-evaluations performed in the Fast Poisson Solver and $\overline{\mathbf{u}}$ represents the space-average velocity, that we aim to correct. The x-axis of the Cartesian system corresponds to flow direction and the velocity is initialized setting $\mathbf{u}(t=0) = (u_{x\infty}, u_{y\infty}, u_{z\infty})$.

Since $\overline{u_x}$ is a spatially constant flux, then $\dfrac{\partial \overline{u_x}}{\partial x} = \dfrac{\partial \overline{u_x}}{\partial y} = \dfrac{\partial \overline{u_x}}{\partial z} = 0$ and the mean vorticity is given by:

$$\overline{\omega_x} = \frac{\partial \overline{u_z}}{\partial y} - \frac{\partial \overline{u_y}}{\partial z}, \qquad \overline{\omega_y} = -\frac{\partial \overline{u_z}}{\partial x}, \qquad \overline{\omega_z} = \frac{\partial \overline{u_y}}{\partial x}. \tag{15}$$

First of all, a correction of the streamwise component of the velocity u_x is necessary in order to impose the correct flux at the inlet. This correction is determined as follows.

4.2.1. Correction for the streamwise velocity u_x

Let I be the inlet rectangular surface of the parallelepipedic computational box, normal to the flow direction, of area $L_y L_z$. L_y and L_z respectively denote the lengths of the computational box in the y and z directions. According to the decomposition $\mathbf{u} = \widetilde{\mathbf{u}} + \overline{\mathbf{u}}$ and knowing that $\overline{u_x}$ is a constant and that the desired flow rate at the inlet is equal to $u_{x\infty} L_y L_z$, one has:

$$\underbrace{\iint_I u_x \, dydz}_{\text{desired flow rate}} = \underbrace{\iint_I \widetilde{u_x} \, dydz}_{\text{calculated flow rate}} + \iint_I \overline{u_x} \, dydz, \tag{16}$$

so

$$\overline{u_x} = u_{x\infty} - \frac{\iint_I \widetilde{u_x}\ dydz}{L_y L_z}, \tag{17}$$

and finally:

$$u_x = u_{x\infty} + \widetilde{u_x} - \frac{\iint_I \widetilde{u_x}\ dydz}{L_y L_z}. \tag{18}$$

Next we need to correct the transverse velocities u_y and u_z in order to recover a non-zero circulation.

4.2.2. Correction for the spanwise velocity u_y

According to relations (15) one has $\overline{u_y} = \overline{\omega_z}x + c_1$, with c_1 a constant value that we aim to evaluate and $\overline{\omega_z} = \dfrac{1}{L_x L_y L_z}\displaystyle\int_D \omega_z\ d\mathbf{x}$, with $L_x L_y L_z$ corresponding to the volume of the computational domain D. From the decomposition $\mathbf{u} = \widetilde{\mathbf{u}} + \overline{\mathbf{u}}$, one therefore concludes that $u_y = \widetilde{u_y} + \overline{\omega_z}x + c_1$. Thus:

$$\iint_I u_y\ dydz = \iint_I \widetilde{u_y}\ dydz + \iint_I \overline{\omega_z}x\ dydz + \iint_I c_1\ dydz. \tag{19}$$

Since the flow rate is desired to be $u_{y\infty}L_y L_z$, then:

$$c_1 = u_{y\infty} - \frac{\iint_I \widetilde{u_y}\ dydz}{L_y L_z} - \overline{\omega_z}x_0, \tag{20}$$

and finally the corrected y-component of the velocity fields stands as:

$$u_y = u_{y\infty} + \widetilde{u_y} + \overline{\omega_z}(x - x_0) - \frac{\iint_I \widetilde{u_y}\ dydz}{L_y L_z}, \tag{21}$$

where x_0 corresponds to the x-coordinate of the inlet surface I in the Cartesian system.

4.2.3. Correction for the transverse velocity u_z

Following the same principle, and according to the relations (15) one obtains $\overline{u_z} = -\overline{\omega_y}x + c_2$ with c_2 a constant value. From the decomposition

$\mathbf{u} = \widetilde{\mathbf{u}} + \overline{\mathbf{u}}$, one gets $u_z = \widetilde{u_z} - \overline{\omega_y} x + c_2$. Finally, mimicking the process used for u_y, one gets:

$$u_z = u_{z\infty} + \widetilde{u_z} - \overline{\omega_y}(x - x_0) - \frac{\iint_I \widetilde{u_z}\, dydz}{L_y L_z}. \tag{22}$$

In order to validate the use of periodic boundary conditions combined with the above corrections, we consider the flow past a 3D sphere at $Re = 300$ in a bounded domain $D = [-2,\ 8.24] \times [-2.56,\ 2.56] \times [-2.56,\ 2.56]$. The target free stream velocity is uniform at the inlet, with $\mathbf{u}_\infty = (1, 0, 0)$. Figure 3 shows upstream isocontours of u_x at the end of the simulation ($T = 75$) in the inlet YZ plane ($x = x_0 = -2$) for two different cases.

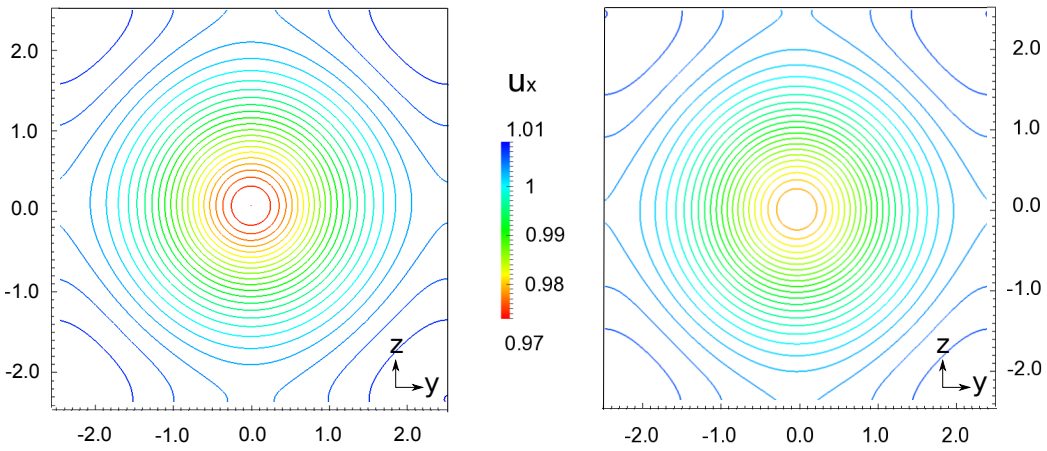

Figure 3: Flow past a 3D sphere: isocontours of the inlet streamwise velocity u_x in the YZ plane when imposing periodic boundary conditions coupled with adapted corrections. (Left picture) The width of the absorption band equals 1. (Right picture) The width of the absorption band equals 2.

In Figure 3 we have plotted the values of the streamwise velocity obtained at the inlet. In the first case (left picture), the absorption band lies from $x_b = 7.24$ to $x_e = 8.24$ and $\alpha = 10$ in the definition of f (eq. 10). In this case the values of u_x lie between 0.973 and 1.009. In the second case (right picture), the absorption band is twice thicker ($x_b = 6.24$, $x_e = 8.24$) and $u_{x\ \text{inlet}} \in [0.977,\ 1.007]$. The actual inlet streamwise velocity thus only shows a maximum relative error of respectively 2.7% and 2.3% for the first and the

second case compared to the target uniform free stream flow ($u_{x\infty} = 1$). Let us also notice the symmetrical patterns of the velocity isocontours. This symmetry is explained by the periodic boundary conditions. Simulations were also performed with a domain twice longer in the x-direction, i.e. $x_b = 17.48$, $x_e = 18.48$ and very similar results were obtained ($u_{x\ \text{inlet}} \in [0.975,\ 1.004]$). Finally, a simulation was carried out in the original domain D with a higher Reynolds number, $Re = 1000$, setting $x_b = 7.24$, $x_e = 8.24$ and comparable results were achieved ($u_{x\ \text{inlet}} \in [0.977,\ 1.004]$). From this study one can conclude that, in view of the speed up obtained by this method, the proposed treatment of the inlet and outlet boundary conditions give satisfactory results.

5. The vortex penalization method

5.1. Numerical discretization

In this section we present the vortex penalization method used to discretize the 3D penalized Vorticity-Transport-Equations (3)-(4). In this study, we will only consider the case of fixed obstacles, which means $\mathbf{u}_b = 0$. The method can be extended to the case of moving bodies along the lines of [19, 20]. Equations (3)-(4) are discretized on a parallelepipedic computational box. The domain is meshed with a uniform Cartesian grid and periodic boundary conditions are prescribed on the walls as described in section 4. These equations are discretized through a viscous splitting algorithm, consisting in solving successively the different operators within the same time iteration [30]. Concerning the main steps of this splitting algorithm, the advection is performed in a semi-Lagrangian way through a vortex method with particle remeshing at each time step to avoid the distortion effects [3]. The penalization equation, the stretching and the diffusion terms as well as the Poisson equation are solved on the underlying grid. Algorithm 1 gives the successive discretization steps.

In this work, the Poisson equation (step (27) in algorithm 1) is solved on the grid using Fast Fourier Transforms (FFT) and periodic boundary conditions. Following section 4, the discretization of this equation is preceded by a vorticity absorption (step (26)) and followed by a velocity correction (step (28)). The diffusion equation (step (32)) is also discretized using FFT-based evaluations. In the following, we will focus on the specific features that contribute to the efficiency of this method for 3D bluff body flows.

Algorithm 1

Initialization

Preliminary velocity field (on grid) $$\mathbf{u}^0 = \mathbf{u}_\infty = (1,0,0) \tag{23}$$

Preliminary vorticity field (on grid) $$\boldsymbol{\omega}^0 = (0,0,0) \tag{24}$$

Vorticity penalization (on grid) $$\boldsymbol{\omega}_\lambda^0 = \boldsymbol{\omega}^0 + \nabla \times \left(\frac{-\lambda\chi\Delta t \mathbf{u}^0}{1+\lambda\chi\Delta t} \right) \tag{25}$$

Marching

Vorticity absorption (on grid) $$\boldsymbol{\omega}^n = \nabla \times [f\mathbf{u}^n + (1-f)\mathbf{u}_\infty] \tag{26}$$

Poisson problem (on grid) $$\Delta \mathbf{u}^n = -\nabla \times \boldsymbol{\omega}^n \tag{27}$$

Velocity correction (on grid) $$\mathbf{u}^{n+1} = \widetilde{\mathbf{u}}^n + \overline{\mathbf{u}}^n \tag{28}$$

Force computation (on grid) $$F = \frac{d}{dt} \int_B (\mathbf{u}^{n+1} - \mathbf{u}_\lambda^{n+1})\, d\mathbf{x} \tag{29}$$

Vorticity penalization (on grid) $$\boldsymbol{\omega}_\lambda^n = \boldsymbol{\omega}^n + \nabla \times \left(\frac{-\lambda\chi\Delta t \mathbf{u}^{n+1}}{1+\lambda\chi\Delta t} \right) \tag{30}$$

Stretching (on grid) $$\frac{\partial \boldsymbol{\omega}^n}{\partial t} = \mathrm{div}(\boldsymbol{\omega}^n : \mathbf{u}^{n+1}) \tag{31}$$

Diffusion (on grid) $$\frac{\partial \boldsymbol{\omega}^n}{\partial t} = \frac{1}{Re}\Delta \boldsymbol{\omega}^n \tag{32}$$

Advection (on particles) $$\frac{\partial \boldsymbol{\omega}^{n+1}}{\partial t} + (\mathbf{u}^{n+1}\cdot\nabla)\boldsymbol{\omega}^{n+1} = 0 \tag{33}$$

Evaluation of Δt_{adapt} (on grid) $$\Delta t_{\text{adapt}}^{n+1} = \frac{\mathrm{LCFL}}{\|\nabla \mathbf{u}\|_\infty^{n+1}} \tag{34}$$

Force computation (step (29))

As explained in section 3, the aerodynamic force is evaluated in 3D using the *change of momentum* equation (7). For this purpose, equation (5) is discretized using a 1^{st} Euler scheme:

$$F = -\frac{1}{\Delta t} \sum_B \left(\mathbf{u}^{n+1} - \mathbf{u}^n\right) h^3, \tag{35}$$

and $\mathbf{u}^{n+1}$ is forced to be equal to the velocity inside the body through an implicit penalization scheme (cf equation (41) in next subsection):

$$F = \frac{1}{\Delta t} \sum_B \left(\mathbf{u}^n - \frac{\mathbf{u}^n}{1 + \lambda \Delta t} \right) h^3 \ = \sum_B \left(\frac{\lambda \mathbf{u}^n}{1 + \lambda \Delta t} \right) h^3, \tag{36}$$

where $\mathbf{u}^n$ corresponds to the non-penalized velocity and h denotes the uniform grid space. This force expression is evaluated on the grid with a midpoint rule. We note that the above equation is consistent with the formulation (7): since in our calculations we have $\lambda = 10^8$ and $\Delta t \geq 10^{-3}$, then $\lambda \Delta t \gg 1$ and (36) gives:

$$F = \sum_B \frac{\mathbf{u}^n}{\Delta t} \, h^3. \tag{37}$$

This is a 1^{st} order discretization of the *change of momentum* equation (7) where $\mathbf{u}_\lambda = 0$.
Let us also notice that, if $\Delta t \to 0$, then one would have:

$$F = \sum_B \lambda \mathbf{u}^n \, h^3, \tag{38}$$

which corresponds to the discretized formulation of the force expression proposed in [25] and obtained by integrating the penalization term on the volume of the body:

$$F = \frac{1}{Re} \int_B \Delta \mathbf{u} \, d\mathbf{x} - \int_B \nabla p \, d\mathbf{x} \approx \int_D \lambda \chi_b \mathbf{u} \, d\mathbf{x}. \tag{39}$$

In the present work one chooses equation (37). The force evaluation is performed immediately before the penalization step in algorithm 1 (step (29)).

Penalization (step (30))

In its velocity-vorticity formulation, the continuous penalization equation reads :

$$\frac{\partial \boldsymbol{\omega}}{\partial t} = -\nabla \times (\lambda \, \chi_b \mathbf{u}). \tag{40}$$

In order to discretize equation (40), we first discretize the penalization equation for the velocity, $\partial_t \mathbf{u} = -\lambda \chi_b \mathbf{u}$. Following [19] this is done using an implicit 1^{st} order Euler scheme:

$$\mathbf{u}^{n+1} = \frac{\mathbf{u}^n}{1 + \lambda \chi_b \Delta t}. \tag{41}$$

This yieds the penalized velocity field that we denote by $\mathbf{u}_\lambda$. We can rewrite the above equation as:

$$\mathbf{u}^{n+1} = \mathbf{u}^n - \left(\frac{\lambda \chi_b \Delta t \ \mathbf{u}^n}{1 + \lambda \chi_b \Delta t} \right), \tag{42}$$

which gives the following conservative expression for the penalized vorticity:

$$\boldsymbol{\omega}^{n+1} = \boldsymbol{\omega}^n - \nabla \times \left(\frac{\lambda \chi_b \Delta t \ \mathbf{u}^n}{1 + \lambda \chi_b \Delta t} \right). \tag{43}$$

A 4^{th} order centered finite-differences scheme is used for the discretization of the curl operator. We notice that the velocity field is not directly penalized in this algorithm. The velocity penalization is implicitly realized through the resolution of the Poisson problem in step (27) of algorithm 1.

Stretching (step (31))

Several formulations may be used to compute the stretching term [1]. In this study we choose the following conservative formulation:

$$\frac{\partial \boldsymbol{\omega}}{\partial t} = \mathrm{div}(\boldsymbol{\omega} : \mathbf{u}), \tag{44}$$

where the notation $\boldsymbol{\omega} : \mathbf{u}$ stands for the tensor of component $\omega_j u_i$. The time integration scheme chosen here to discretize this equation is the commonly used 3^{rd} order Runge-Kutta TVD (Total Variation Diminishing, i.e. non extra oscillations) scheme [31]. With this time discretization, the velocity field involved in the divergence operator is not modified. The divergence operator is discretized through a 4^{th} order centered finite-differences scheme on the grid.

Particle advection and remeshing procedure (step (33))

The semi-Lagrangian advection in the 3D case is performed using a 1^{st} order directional splitting approach [24, 10]. This technique consists in solving the convection/remeshing problem direction by direction. In other words one has to solve here three different mono-dimensional problems.

First, one solves the following differential equations to update the new positions of particles at time t^{n+1} from the grid positions x_i^n and the first component u_1 of velocity field u^n at time t^n:

$$\begin{cases} \dfrac{dx_p}{dt} = u_1(x_p), & t \in [t^n,\ t^{n+1}] \\ x_p^n = x^n. \end{cases} \tag{45}$$

A 2^{nd} order Runge-Kutta scheme is used for the resolution of this equation. Once all the particles have been pushed in the same direction, they are remeshed on the grid, in this direction. Then one proceeds to the advection-remeshing in the second and third direction. The kernel chosen here is $\Lambda_{4,2}$ [32, 10]. Its 1D support includes 6 points, it satisfies 4 moment conditions and is twice differentiable. It yields a second order approximation to the advection equation. It is defined by the following formulas:
$\Lambda_{4,2}(x) =$

$$\begin{cases} 1 - \frac{5}{4}|x|^2 - \frac{35}{12}|x|^3 + \frac{21}{4}|x|^4 - \frac{25}{12}|x|^5 & 0 \leq |x| < 1 \\ -4 + \frac{75}{4}|x| - \frac{245}{8}|x|^2 + \frac{545}{24}|x|^3 - \frac{63}{8}|x|^4 + \frac{25}{24}|x|^5 & 1 \leq |x| < 2 \\ 18 - \frac{153}{4}|x| + \frac{255}{8}|x|^2 - \frac{313}{24}|x|^3 + \frac{21}{8}|x|^4 - \frac{5}{24}|x|^5 & 2 \leq |x| < 3 \\ 0 & |x| \geq 3 \end{cases}$$

where $|x|$ denotes the distance between the particle and a given grid point. From this formula, one can evaluate direction-by-direction the weights collected by each grid point involved in the kernel support. In each direction, the remeshing scheme yields :

$$\omega_i^{n+1} = \sum_p \omega_p^n \Lambda_{4,2}\left(\frac{x_p^{n+1} - x_i}{h}\right). \tag{46}$$

This particle convection/remeshing algorithm allows a significant reduction of the computational efforts compared to the more traditional remeshing based on tensor product formulas.

Adaptive time step (step (34))

In particle methods, the non-linear stability of the convection scheme is ensured under the following condition on the time step:

$$\Delta t_{\text{adv}} \leq \frac{\text{LCFL}}{\|\nabla \mathbf{u}\|_\infty}, \tag{47}$$

where the Lagrangian CFL must satisfy LCFL ≤ 1. As rigorously analyzed in the convergence proof [10], this Lagrangian CFL is the appropriate condition under which consistency and stability of the remeshed particle method can be guaranteed. This Lagrangian stability condition imposes that particles

trajectories do not cross. One can notice here that the time step in not constrained by the grid size or the distance between the particles but only by the flow strain, which often provides larger time steps compared to Eulerian grid-based schemes. In the present study, the time-step is updated at each iteration using the condition (47) with LCFL = 1/8. Except at the initial stage of the simulations, when strong vorticity layers develop around the obstacle, we observed that the time-step rapidly settles at a roughly constant value.

5.2. Implementation and library description

The vortex penalization method is implemented in a library which uses object oriented programming techniques in order to reach a high level of modularity, with a strong focus on usability and flexibility. Our goal is to enable the user to launch indifferently sequential or parallel (MPI) simulations. We use Python as an abstraction framework and the high level of abstraction provided by this language allows to conceal from the user the parallel paradigms and the low level implementations of the numerical algorithms. Concretely, the user only needs to describe his problem with high level components, mathematical operators, problem variables and physical domain description, and then has to choose the available numerical methods and algorithms, or develop his own modules, according to his needs. This abstraction framework enables us to develop a library that is portable to various kinds of modern computer architectures. More information about this library can be found in [10], where a special attention is made on the capability of the presented software to perform hybrid CPU-GPU numerical simulations. In the following, the computations are only CPU-based.

6. Numerical results for bluff body flows

In this section we present the numerical results obtained with the present method. Its convergence and accuracy are numerically analyzed for three-dimensional bluff body flows. The numerical results presented in this section are based on DNS simulations. Laminar and transitional flows are considered for two distinct obstacles, namely the sphere and the hemisphere. In the hemisphere case, the bluff-surface faces the upstream flow and the flat one is oriented downstream. In both cases the non-dimensional diameter d of the obstacle and the free stream velocity are set equal to 1. The obstacles are centered at the origin of the computational box.

6.1. Numerical setup

In all our simulations the size of the computational box was chosen large enough so that the presence of the artificial boundaries was found to be negligible. A careful convergence study with respect to the domain size has been performed in [9] for flow past a 2D circular cylinder using vortex methods. It demonstrates that a domain extending to about 6 cylinder diameters downstream is sufficient to provide reliable flow diagnostics. In the present work, the additional zone used for the absorbing boundary condition accounts only for about 10% of the total size (and thus of the total computational cost). In the subsequent simulations, the size of the domain is set to $D = [-2,\ 8.24] \times [-2.56,\ 2.56] \times [-2.56,\ 2.56]$. The computational domain D and the geometrical setup are shown in Figure 4 for both obstacles. The whole domain is discretized with a uniform Cartesian grid.

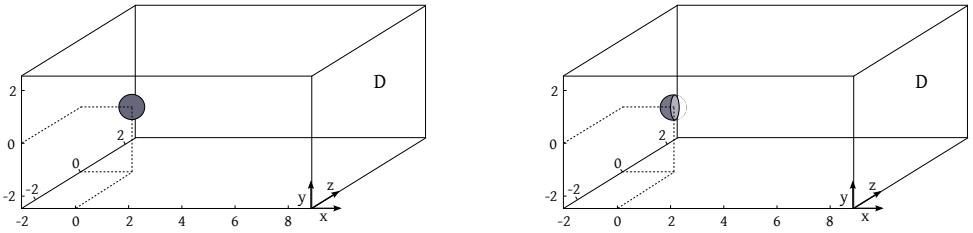

(a) Flow past a sphere (b) Flow past a hemisphere

Figure 4: Computational domain D.

For each of the different flows considered in this section, a convergence study will be carried out and comparisons of our results with respect to numerical and experimental references will be given.

6.2. Flow past a 3D sphere

Flow past a sphere is a common benchmark to validate the accuracy of a numerical method and to prove its capability to correctly model 3D bluff body flows.

6.2.1. Grid convergence study

A grid convergence study is performed in the context of flow past a 3D sphere at $Re = 300$. It involves four mesh sizes: $h = 0.08$, $h = 0.04$, $h = 0.02$ and $h = 0.01$, which correspond to a number of grid points ranging from $128 \times 64 \times 64$ to $1024 \times 512 \times 512$ in the domain D. Convergence orders

are determined by computing the L^1, L^2 and L_∞ norms of the error of two different flow quantities, namely the enstrophy $Z = \int_D |\boldsymbol{\omega}|^2 \, d\mathbf{x}$ and the drag coefficient C_D, with respect to the best resolved case ($h = 0.01$):

$$e(t) = \; || \; q_{\text{best resolved}}(t) - q(t) \; ||, \tag{48}$$

where the quantity q either denotes the drag coefficient C_D or the enstrophy Z. In the particular context of this grid-convergence study, the time-step had to decrease proportionally to the grid size. Instead of (47), we used the following criterion to evaluate it:

$$\Delta t^n_{\text{adapt}} = \frac{\text{CFL} \cdot h}{\max\limits_{1 \le i \le 3} |u_i|}, \qquad \text{with CFL} = 0.5. \tag{49}$$

Figure 5 indicates that the method exhibits around second order convergence regarding drag coefficient (1.95 for L^1, 2.46 for L^2 and 1.98 for L_∞) and between first and second order convergence for the enstrophy (0.93 for L^1, 1.35 for L^2 and 1.06 for L_∞).

The asymptotic mean values of the drag coefficient and the enstrophy are given by Table 1 for each mesh size. Based on Table 1, one can consider that the grid convergence is roughly achieved for $h \le 0.04$.

	$Re = 300$	
Grid	$\bar{c_D}$	$\bar{Z}$
$h = 0.08$	0.732	64.8
$h = 0.04$	0.679	66.5
$h = 0.02$	0.673	67.7
$h = 0.01$	0.676	68.9

Table 1: Convergence study for flow past a sphere at $Re = 300$. $\bar{C_D}$ and $\bar{Z}$ respectively denote the mean values of drag coefficient and enstrophy.

The next simulations of incompressible flows past a 3D sphere at $Re = 300$ will be performed with a mesh size set to 0.02 in order to better capture the boundary layer.

6.2.2. Flow analysis and validations

Flow past a 3D sphere has been widely studied numerically and experimentally which allowed to precisely determine the different flow regimes. Following the studies of [33] and the description given in [4], we recall the regimes related to Reynolds numbers ranging from 0 to a few thousands:

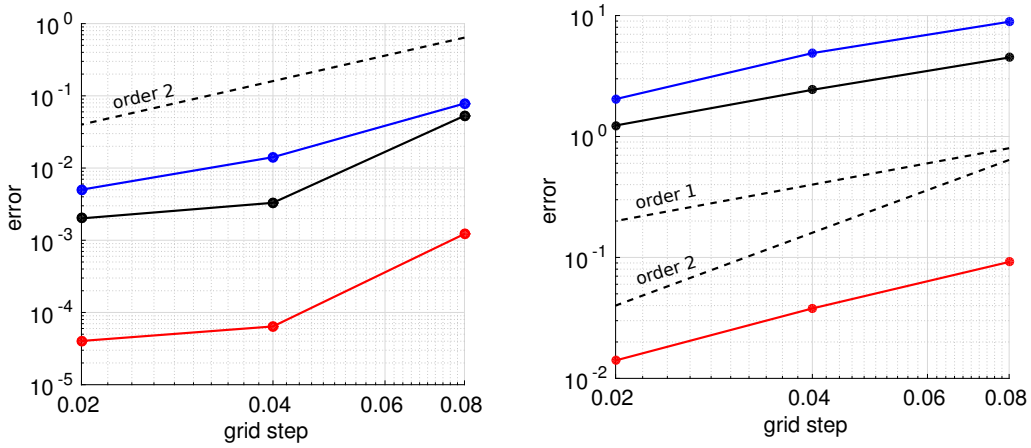

(a) (b)

Figure 5: Grid-convergence study for flow past a sphere at $Re = 300$. The errors e_{L^1} (black), e_{L^2} (red) and e_{L^∞} (blue) are plotted against the grid step. (a) Convergence of the drag coefficient (b) Convergence of the enstrophy.

- $Re < 210$ - 212: the flow is steady and axisymmetric.
  An axisymmetric separation bubble exists at the back of the sphere with zero lift force.

- 210 - 212 $< Re <$ 270 - 290: the flow is steady and planar-symmetric.
  A pair of planar-symmetric vortical structures appears in the wake.

- 270 - 290 $< Re <$ 350 - 375: the flow is unsteady, time periodic and planar-symmetric. The wake is characterized by a cyclic shedding of ring vortices, with planar-symmetry.

- 350 - 375 $< Re <$ 800: the flow is unsteady, non-periodic and fully asymmetric.

- $Re > 800$: the flow is unsteady, non-periodic, asymmetric and a Kelvin-Helmholtz instability occurs in the shear layer, propagating in the wake. The latter becomes fully turbulent, characterized by the emergence of small scales.

In the sequel, we propose validation studies for two Reynolds numbers corresponding to clearly distinct regimes: $Re = 300$ and $Re = 1000$.

Flow past a sphere at $Re = 300$

We first present the results obtained at $Re = 300$. The simulation setup is the following: the 3D computational box $D = [-2,\ 8.24] \times [-2.56,\ 2.56] \times [-2.56,\ 2.56]$ is meshed by an uniform $512 \times 256 \times 256$ Cartesian grid (corresponding to $h = 0.02$). As in [4], a perturbation is addressed to the uniform upstream flow between the non-dimensional time $T = 3$ and $T = 4$, in order to trigger the instability. This perturbation is applied on the y component of the velocity and stands as $u_{y\infty} = \sin(\pi(T-3))$. The time step is defined according to equation (47). It is approximately equal to 0.011 all along the simulation. The penalization parameter λ is set to 10^8.

Table 2 compares the values of the drag and vertical lift coefficients as well as the Strouhal number obtained using the present method with results in literature.

	$Re = 300$		
Authors	$\bar{c_D}$	$\bar{c_L}$	S_t
Roos & Willmarth * [34]	0.629	-	-
Johnson & Patel [33]	0.656	-0.069	0.137
Tomboulides & Orszag [35]	0.671	-	0.136
Constantinescu & Squires [36]	0.655	-0.065	0.136
Kim & Choi [37]	0.657	-0.067	0.134
Ploumhans et al. [4]	0.683	-0.061	0.135
Present work	0.673	-0.066	0.133

Table 2: Comparison of drag and lift coefficients and Strouhal number for flow past a sphere at $Re = 300$. Star notation (*) refers to experimental results.

As the table shows, our results coincide well with these references. Figure 6 depicts the ω_z and ω_x isocontours for every quarter period of a shedding cycle. The contours of the streamwise (ω_x) and spanwise (ω_z) components of the vorticity obtained with the present method are compared with those published by [4]. As can be observed on the figure, the vortical features are in very good agreement with the reference results. Moreover, one can notice that a true periodic regime is attained (the snapshots in Figures 6a and 6b depict the vorticity field at five equispaced times within one shedding period) and that the wake is perfectly symmetric in the XZ plane (see the ω_x isocontours in the XZ plane in Figure 6b). These observations confirm the description of the flow regime corresponding to Reynolds 300 thoroughly investigated by

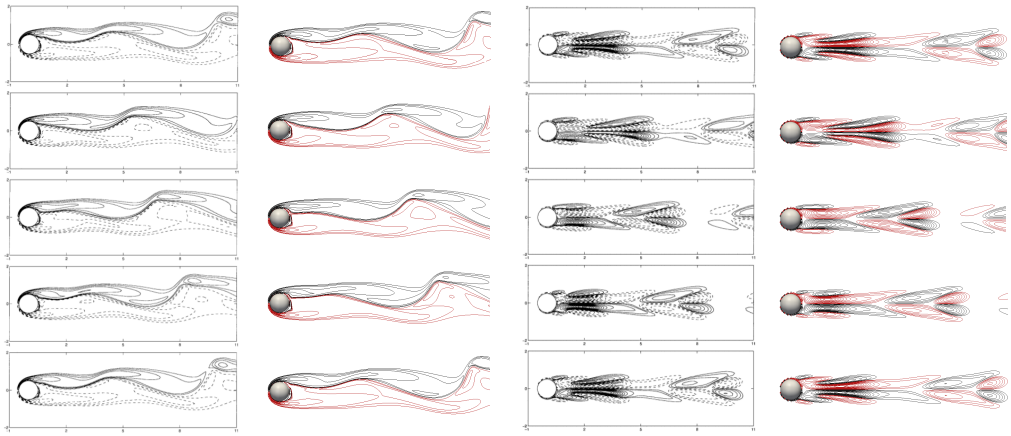

(a) Isocontours of ω_z in the XY plane (b) Isocontours of ω_x in the XZ plane

Figure 6: Vorticity isocontours for flow past a sphere at $Re = 300$ for every quarter period of a shedding cycle. Comparison between [4] (left columns) and present results (right columns).

[33, 35] and given at the beginning of this section. Finally, Figure 7 depicts 3D views of the vorticity norm $|\boldsymbol{\omega}|$ resulting from simulations performed in a longer computational domain, $D = [-2,\ 18.48]\times[-2.56,\ 2.56]\times[-2.56,\ 2.56]$. One can notice in particular that, at $Re = 300$, the vortex shedding from a sphere does not symmetrically alternate along the flow direction (XY plane), where the top eddies are much stronger than the bottom ones (Figure 7a). This observation confirms the one made by [37] and corresponds to the fact that the vertical lift coefficient $\bar{C_L}$ is non-zero (see Table 2).

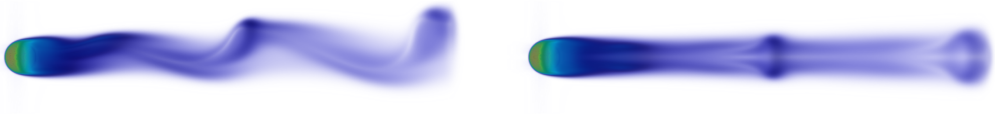

(a) XY plane (b) XZ plane

Figure 7: 3D instantaneous vorticity norm $|\boldsymbol{\omega}|$ at $T = 72$ for flow past a sphere at $Re = 300$.

Flow past a sphere at $Re = 1000$

The flow analysis at $Re = 1000$ is now considered. The simulation is

performed on an uniform $1024 \times 512 \times 512$ Cartesian grid (corresponding to $h = 0.01$). A perturbation is applied between $T = 3$ and $T = 4$ on the y component of the velocity, defined by $u_{y\infty} = 0.1 \sin(\pi(T-3))$. The adaptive time step returns a value roughly equal to $\Delta t = 0.005$, which corresponds to a CFL number equal to 0.6. The penalization parameter λ is fixed to 10^8.

A plot of the time average streamwise velocity u_x along the centerline is given in Figure 8a. The results obtained with the present method are compared to those of [35] together with the experimental data of [38] at $Re = 960$. It can be seen that the length of the recirculation zone, characterized by negative u_x values, obtained in the present case (1.5 diameters) is similar to the one obtained in [35] (approximately 1.7 diameters). Furthermore, the u_x values for $x/d \geq 2$ are in a very good agreement with other numerical and experimental studies ([35] and [38]) and show the accuracy of the present method. The three experimental and numerical results are however slightly different for smaller x/d values. As the number of points in the boundary layer are almost the same for both numerical methods (3.3 points in the present case and 3.5 in [35]) these discrepencies may be due to the interpolation errors in the boundary layer that contains very high velocity gradients. Moreover, some experimental errors at $x/d < 2$ also could be induced during the measurements.

Concerning the time evolution of force coefficients, Figure 8b shows that the time evolution of the drag coefficient C_D and the vertical lift coefficient C_L coincide with the one found by [4]. As emphasized in [4], although the prescribed perturbation is symmetric, the flow quickly looses its plane symmetry. This is confirmed by Figure 9, giving the evolution of the force coefficients for a larger time range. The side lift force coefficient C_S is non-zero and shows significant variations which are actually in the same order of magnitude as C_L. Concerning the drag coefficient C_D, the mean value obtained in the present study is 0.485, which agrees well with the numerical values reported by [39] and [40], respectively equal to 0.46 and 0.478. Isocontours of $|\boldsymbol{\omega}|$ in the near wake are depicted in the XY and XZ plane for early times, respectively in Figure 10a and 10b. They are compared to those of [4]. These figures, which show a good agreement, reveal that the flow is initially symmetric in the XZ plane. However, as highlighted by Figure 11, the near wake becomes asymmetric at $T = 18$. The same value of T is reported by [4]. This loss in planar-symmetry increases in time and is perfectly clear at $T = 40$ (see Figures 11 and 12). These observations on the wake symmetry are directly related to the C_S time evolution given in Figure 9 where, from

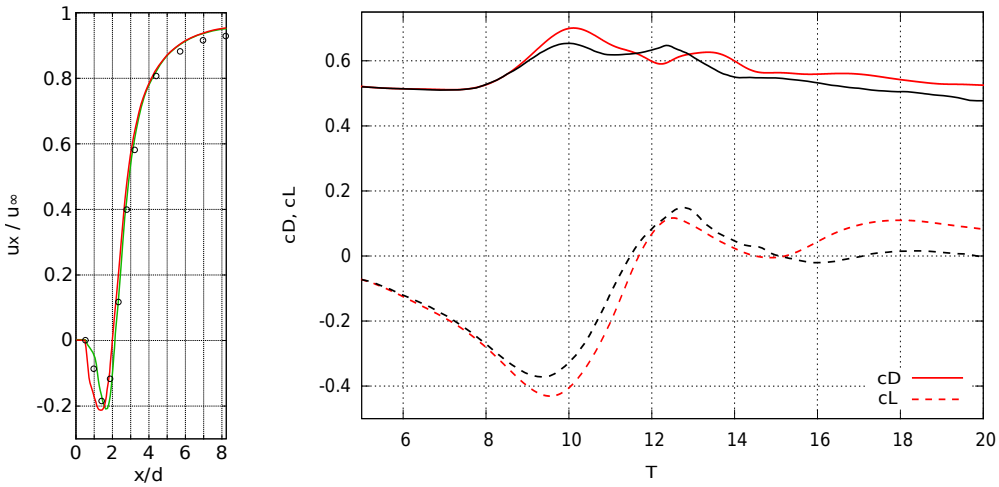

Figure 8: Flow past a sphere at $Re = 1000$: (a) Average streamwise velocity u_x along the x-axis: comparison of the present results (red curve) with numerical results [35] (green curve) and experimental data [38] at $Re = 960$ (black circles). (b) C_D (solid lines) and C_L (dashed lines) time evolution: comparison of the present results (red curves) with [4] (black curves).

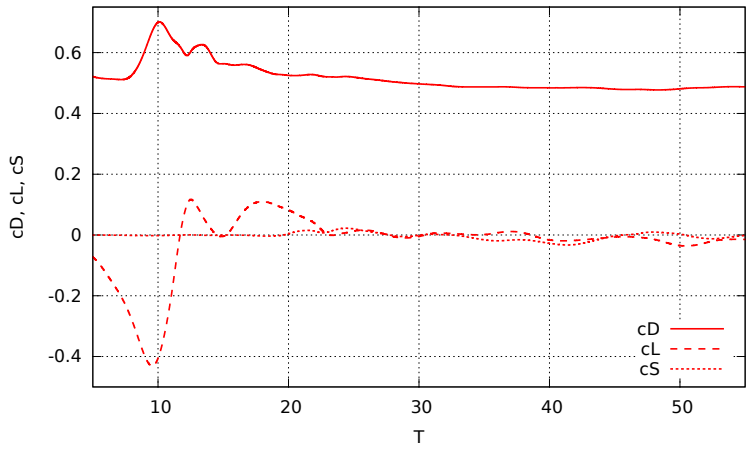

Figure 9: C_D (solid line), C_L (dashed line) and C_S (dotted line) time evolution for flow past a sphere at $Re = 1000$.

$T \simeq 18$, C_S is shown to be non-zero.

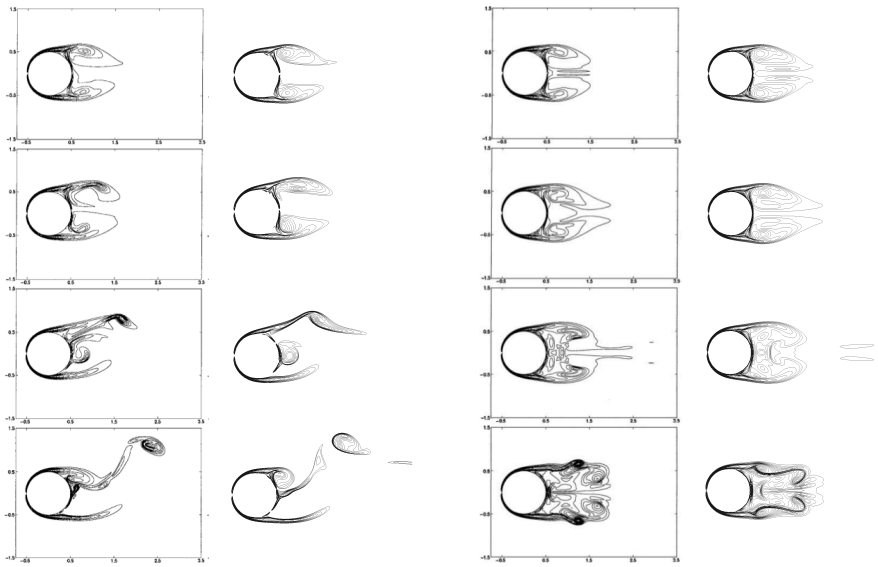

(a) in the XY plane (b) in the XZ plane

Figure 10: Isocontours of $|\boldsymbol{\omega}|$ for flow past a sphere at $Re = 1000$. Comparison between [4] (left columns) and present results (right columns) at $T = 6$, 8, 10, 12.

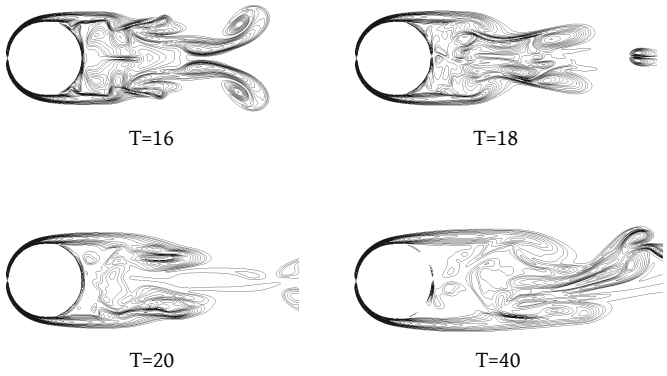

Figure 11: Isocontours of $|\boldsymbol{\omega}|$ in the XZ plane for flow past a sphere at $Re = 1000$. The near wake becomes asymmetric from $T = 18$.

(a) XY plane (b) XZ plane

Figure 12: 3D instantaneous vorticity norm $|\boldsymbol{\omega}|$ at $T = 40$ for flow past a sphere at $Re = 1000$.

6.3. Flow past a 3D hemisphere

Hemispherical bodies correspond to configurations that may be used in several engineering applications. In a previous work [22], this geometry was used to investigate drag reduction around the side view mirror of a ground vehicle. Due to the presence of a flat back wall with sharp edges, the flow past a hemisphere is a steeper problem compared to the flow past a sphere and is therefore challenging from a numerical point of view. Vortex methods adapted to geometry singularities have been proposed in two dimensions in [13]. The purpose of the present work is in particular to measure to which extent penalization methods can handle this type of singularity in three dimensions, at low and moderate Reynolds numbers. The refinement study proposed in the following section proves that the accuracy of the penalization method for sharp eddy geometries is the same as the one obtained for smooth bluff bodies.

6.3.1. Grid convergence study

A grid convergence study is performed for flow past a 3D hemisphere at $Re = 300$. As for the sphere, four different mesh sizes are considered for this convergence study and the time step is defined according to equation (49). The order of convergence for the drag coefficient is found to be 1.80 for L^1, 2.23 for L^2, 1.48 for L_∞ (Figure 13a) and 0.95 for L^1, 1.49 for L^2, 1.23 for L_∞ concerning the enstrophy (Figure 13b). These convergence orders are very similar to those found for the sphere in the previous section. They are complemented by Table 3, giving the converged mean values of the two flow quantities at $Re = 300$. Here again, on the basis of these results one may consider that the grid convergence is roughly obtained by setting $h = 0.04$.

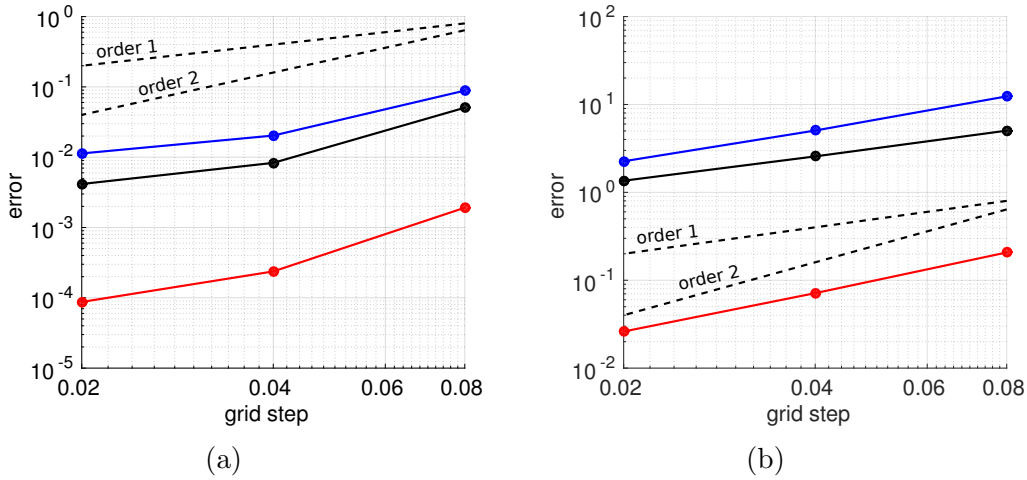

Figure 13: Grid-convergence study for flow past a hemisphere at $Re = 300$. The errors e_{L^1} (black), e_{L^2} (red) and e_{L^∞} (blue) are plotted against the grid step. (a) Convergence of the drag coefficient. (b) Convergence of the enstrophy.

	$Re = 300$	
Grid	$\bar{c_D}$	$\bar{Z}$
$h = 0.08$	0.787	73.4
$h = 0.04$	0.725	73.0
$h = 0.02$	0.721	73.3
$h = 0.01$	0.725	74.0

Table 3: Convergence study for flow past a hemisphere at $Re = 300$. $\bar{C_D}$ and $\bar{Z}$ respectively denote the mean values of drag coefficient and enstrophy.

6.3.2. Flow analysis and validations

To our knowledge there are only few experimental and numerical results devoted to the problem of flow past a 3D hemisphere. This section is based on the study carried out by Kim & Choi [41], who investigated in details the behavior of flows past a hemisphere at different Reynolds numbers, ranging from 100 to 300. In their study, the authors report the following flow regimes:

- $Re = 100, 130, 150, 170$: the flow is steady and axisymmetric.
- $Re = 180, 190$: the flow is steady and planar-symmetric.
- $Re = 200, 210$: the flow is unsteady, time periodic and asymmetric.

- Re = 220, 250, 270: the flow is unsteady, time periodic and planar-symmetric.
- Re = 280, 300: the flow is unsteady, non-periodic and asymmetric.

Let us first draw some comparisons between these flow regimes and the ones of the sphere, listed in the previous section. One can notice that steady flows over a hemisphere are very similar to those over a sphere, even if the transitions between the different flow regimes occur at lower Reynolds numbers in the hemisphere case. Indeed, as explained in [41], the steady axisymmetric flow is characterized by an axisymmetric recirculation zone behind the hemisphere, while for the steady planar-symmetric flow two streamwise vortical structures are formed in the wake. However, according to the authors, an important difference exists between the unsteady flows past a hemisphere and those past a sphere. We indeed notice that when $220 \leq Re \leq 270$, the flow past a hemisphere recovers planar-symmetry while for lower Reynolds number (Re = 200, 210), it was totally asymmetric. This behavior is not observed in the case of the sphere.

Flow past a hemisphere at low Reynolds numbers

In this validation study we will focus on three values of the Reynolds number, corresponding to different unsteady flow behaviors: $Re = 200$, 250, and 300. These Reynolds numbers are also studied in details in [41]. For each simulation, we consider a $512 \times 256 \times 256$ Cartesian grid (corresponding to $h = 0.02$). As for the sphere, the flow instability is triggered by a perturbation imposed between $T = 3$ and $T = 4$.

The flow at $Re = 200$ is first considered. Figure 14a shows the time evolution of the drag and lift coefficients, which are compared to those obtained by [41]. First, one can notice a very good agreement between the different results, which is confirmed by the first lines of Table 4 giving the mean values of the force coefficients at $Re = 200$. Concerning the Strouhal number, one can see in our case and in the reference results that the Strouhal based on the lift is half the one based on the drag. Finally, we focus on the side lift coefficient C_S. At $Re = 200$ the time average of this coefficient is not zero, which corroborates the fact that the flow does not maintain the planar-symmetry. This statement is confirmed by Figure 14b depicting the vorticity norm $|\boldsymbol{\omega}|$ at two different times, where one can see that the wake is not symmetric in

$Re = 200$	$\bar{c_D}$	$\bar{c_L}$	$\bar{c_S}$	St_{lift}	St_{drag}	
Kim & Choi [41]	0.790	0.0 ± 0.024	0.049	0.128	0.256	
Present	0.805	0.003 ± 0.025	0.043	0.129	0.257	
$Re = 250$	$\bar{c_D}$	$\bar{c_L}$	$\bar{c_S}$	St_{lift}	St_{drag}	
Kim & Choi [41]	0.742	0.0 ± 0.05	0.0	0.127	0.254	
Present	0.757	0.0 ± 0.05	0.0	0.128	0.256	
$Re = 300$	$\bar{c_D}$	$\bar{c_L}$	$\bar{c_S}$	St_{lift}	St_{drag1}	St_{drag2}
Kim & Choi [41]	0.715	0.0 ± 0.062	0.0	0.135	0.04	0.270
Present	0.729	-0.002 ± 0.063	-0.0016	0.134	0.04	0.270

Table 4: Comparison of mean drag and lift coefficients as well as Strouhal numbers for flow past a hemisphere at $Re = 200$, 250 and 300.

the plane XZ at this Reynolds number.

Let us now focus on flow past a hemisphere at $Re = 250$. Figure 15a and Table 4 show that the present outcomes coincide well with the reference results. As for the flow at $Re = 200$, the shedding frequency is equal to the frequency of the lift ($St_{\text{lift}} = 0.128$) and half the frequency of the drag ($St_{\text{drag}} = 0.256$). Finally, Figure 15b confirms that the flow at $Re = 250$ recovers the symmetry in the XZ plane. This observation explains the zero time average side lift coefficient ($\bar{C_S} = 0$) read in Table 4.

At $Re = 300$, according to Figure 16a the flow has a more complex behavior, showing drag and lift coefficients with complicated variations in time. The vorticity norm reported in Figure 16b also highlights the absence of any planar-symmetry, as expected. On the other hand, Table 4 reveals that, at this regime, there co-exist two distinct values of the Strouhal number based on the power spectrum of the drag. The lower frequency ($St_{\text{drag1}} = 0.04$) is due to the large-scale instability of the wake, while the higher frequency ($St_{\text{drag2}} = 0.270$) is attributed to the small-scale instabilities caused by the separation of the shear layer. The St_{drag2} value is still approximately equal to twice the dominant frequency of the lift ($St_{\text{lift}} = 0.138$). One can also remark in Table 4 that the time average lift coefficient $\bar{C_L}$ is zero (like for $Re = 200$ and $Re = 250$), which is not the case for flow past a sphere at $Re = 300$ (see $\bar{C_L}$ in Table 2). This difference can be explained by the discrepancy in the process of vortex shedding. Indeed, as can be seen in Figure 16b, in the case of a hemisphere the vortices shed alternatively with the same strength in the flow direction (XY plane), leading to $\bar{C_L} = 0$. On the contrary, at

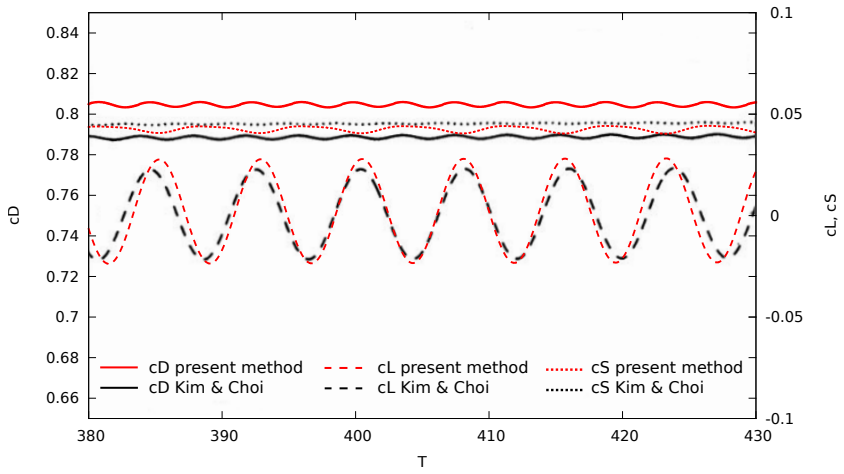

(a) Comparison of the time evolution of the force coefficients with the numerical results of [41].

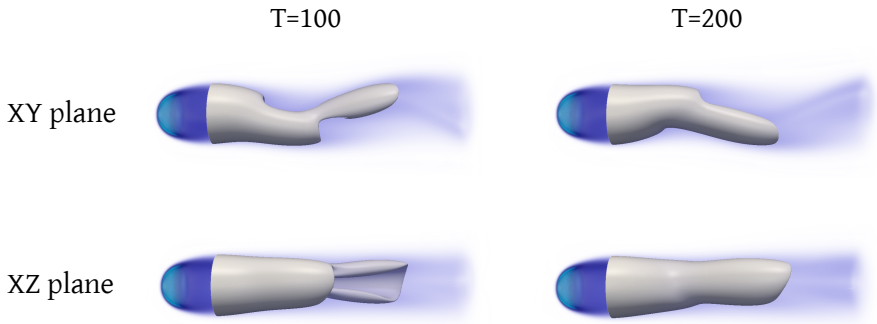

(b) Instantaneous 3D vortical structures with isocontour $|\boldsymbol{\omega}| = 0.8$.

Figure 14: Flow past a hemisphere at $Re = 200$.

the same Reynolds number, we shown in the previous section that the vortex shedding from a sphere was not alternating symmetrically (see Figure 7a).

Flow past a hemisphere at $Re = 1000$

Our last investigation is performed at $Re = 1000$. To to our knowledge, no study has been carried out experimentally or numerically at such regime, and more generally at a Reynolds number larger than $Re = 300$. On the basis of the grid refinement study presented in section 6.3.1 we have chosen for this case a grid-step value $h = 0.01$. All the other numerical parameters

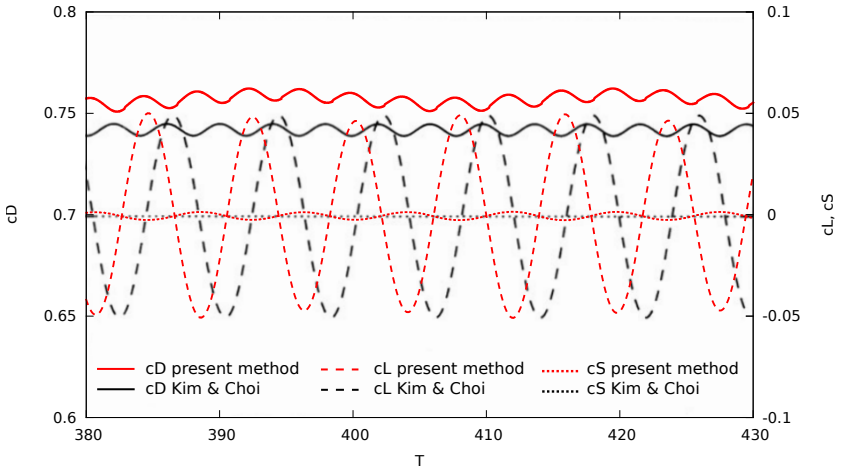

(a) Comparison of the time evolution of the force coefficients with the numerical results of [41].

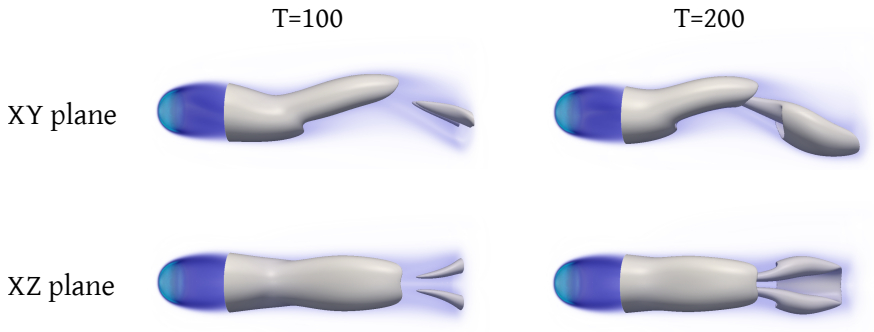

(b) Instantaneous 3D vortical structures with isocontour $|\boldsymbol{\omega}| = 0.8$.

Figure 15: Flow past a hemisphere at $Re = 250$.

used for this simulation are the same as the one chosen for the sphere at the same Reynolds number (see section 6.2.2). The results presented in Figure 17 indicate that the characteristics of the flow past a hemisphere at $Re = 1000$ are similar to the one observed in the case of the sphere at the same regime, in the sense that it is unsteady, non-periodic and asymmetric. Figure 17a shows the streamwise velocity u_x along the centerline, averaged on the time range $T = [60,\ 100]$. Although this mean velocity profile is evaluated on a later time range, one can nevertheless notice that it is comparable to the one of the sphere (see Figure 8a), with in particular a recirculation zone extending from the rear back of the obstacle to $x \simeq 2$. The time history of

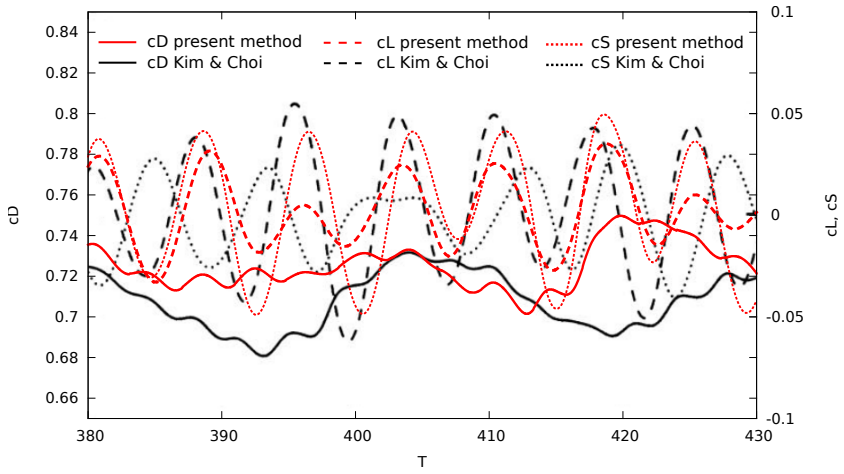

(a) Comparison of the time evolution of the force coefficients with the numerical results of [41].

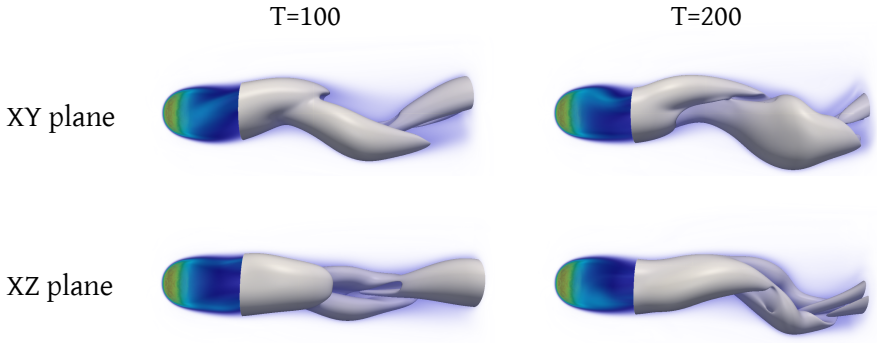

(b) Instantaneous 3D vortical structures with isocontour $|\boldsymbol{\omega}| = 0.8$.

Figure 16: Flow past a hemisphere at $Re = 300$.

the force coefficients is reported in Figure 17b. It shows that from $T \simeq 55$ the wake becomes chaotic and is characterized by important and non-periodic variations of the side lift coefficient C_S. Three-dimensional representations of the turbulent wake are given in Figure 17c at $T = 60$ and $T = 100$. Figure 17c also reports the time averages of the vorticity magnitude between $T = 70$ and $T = 110$ in the XY and XZ plane, highlighting the chaotic feature of the wake. In particular, we remark in both planar section on the right pictures of Figure 17c that a large recirculation area with low vorticity values exists behind the hemisphere, followed by an important zone characterized by high vorticity values.

We note here that, under the same initial conditions and identical numerical parameters, the wake of the hemisphere looses its symmetry in the XZ plane much later than the one of the sphere ($T \simeq 18$, see Figure 11). Figure 18 depicts the isocontours of the streamwise vorticity past a hemisphere in the XZ plane at different times. One can verify in particular that, as suggested by the evolution of the side lift coefficient C_S (see Figure 17b), the wake looses its symmetry between $T = 40$ and $T = 60$. The retarded asymmetric behavior can be explained by the flat back wall of the hemisphere and seems triggered by the insight of secondary instabilities in the shedding shear areas.

7. Computational resources

The simulations presented in this paper were performed on a cluster made of bi-Xeon Sandy-Bridge cores. Table 5 gives the numerical setup, the resources and the CPU time-to-solution for different bluff body flows analyzed in this work. The simulations presented in this paper were realized in the domain $D = [2,\ 8.24] \times [-2.56,\ 2.56] \times [-2.56,\ 2.56]$. The different t_{end} values reported in the table and corresponding to the non-dimensional final time of the simulations were chosen according to the reference test-cases we wanted to compare with. Δt_{adapt} denotes the mean of the non-dimensional adaptative time step. This mean value is calculated on the time range $[\tilde{t},\ t_{\text{end}}]$, where $\tilde{t}$ denotes the time from which the flow regime is established.
For simulations performed at $Re = 300$, the allocated memory was less than 2.7 Gbytes and for simulations carried out at $Re = 1000$, it did not exceed 21 Gbytes. The CPU time-to-solution shown in this table correspond to a CPU time of about 40 seconds per time step on 64 cores for the high resolution cases with $N = 1024 \times 512^2$, and of about 8 seconds per time step on 32 cores for the lower resolution cases with $N = 512 \times 256^2$. This indicates a weak scalability in this range of resolutions around 80%.
Figure 19 gives the percentage of the different stages implied in the resolution of the 3D penalized Vorticity-Transport-Equations (3)-(4), in one simulation time step for the execution on 1 core. In particular, one can notice that the FFT grid-based Poisson solver only represents 5% of the total CPU cost of one time step.

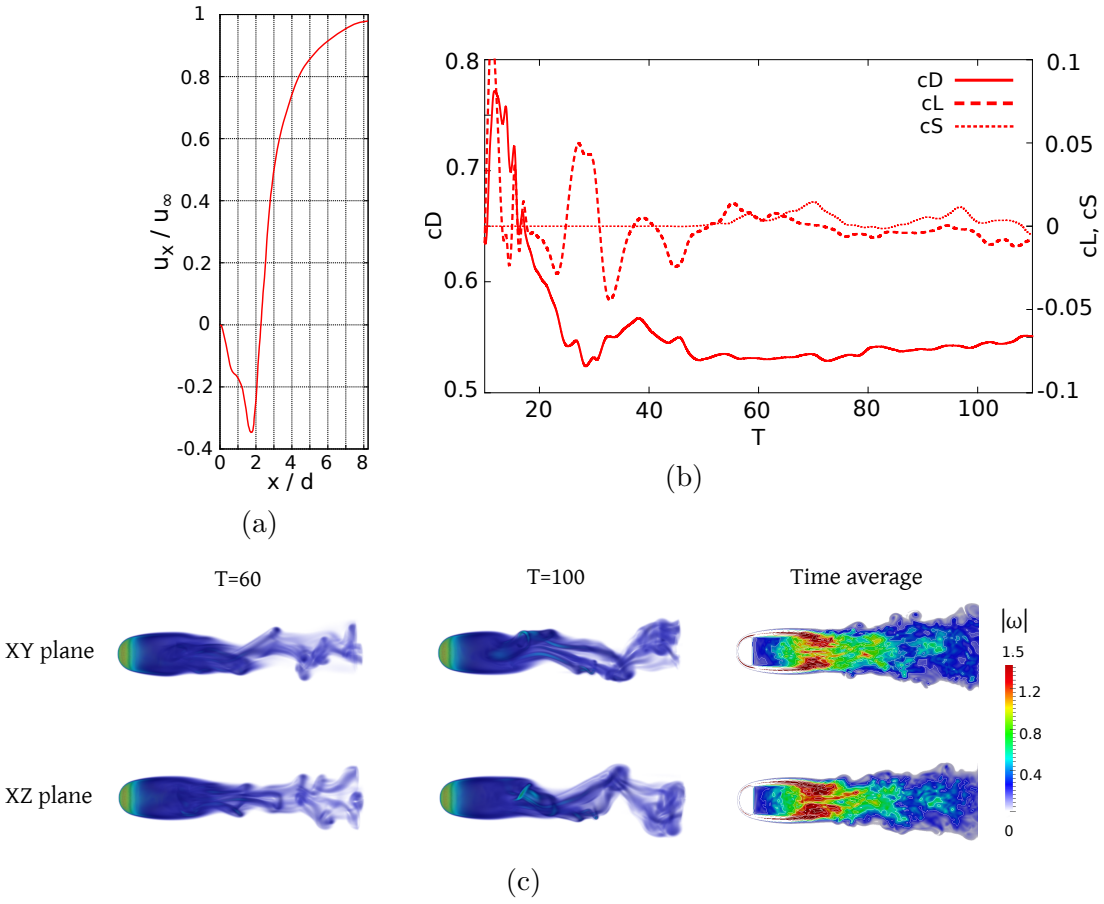

Figure 17: Flow past a hemisphere at $Re = 1000$. (a) Average streamwise velocity u_x along the x-axis. (b) Time evolution of the force coefficients. (c) Instantaneous vortical structures at $T = 60$ and $T = 100$ and time average of vorticity magnitude between $T = 70$ and $T = 110$ in the XY and XZ plane.

8. Conclusion

In this work, a vortex penalization technique has been employed to simulate three-dimensional bluff body flows. The method combines the simplicity of the penalization technique and the robustness of remeshed particle methods. The penalization approach allows the use of simple Cartesian grids and associated fast Poisson solvers to compute velocity fields. For this particular case of flows where the boundary conditions are either periodic or prescribed through upstream flows and free downstream flow, we showed that it is pos-

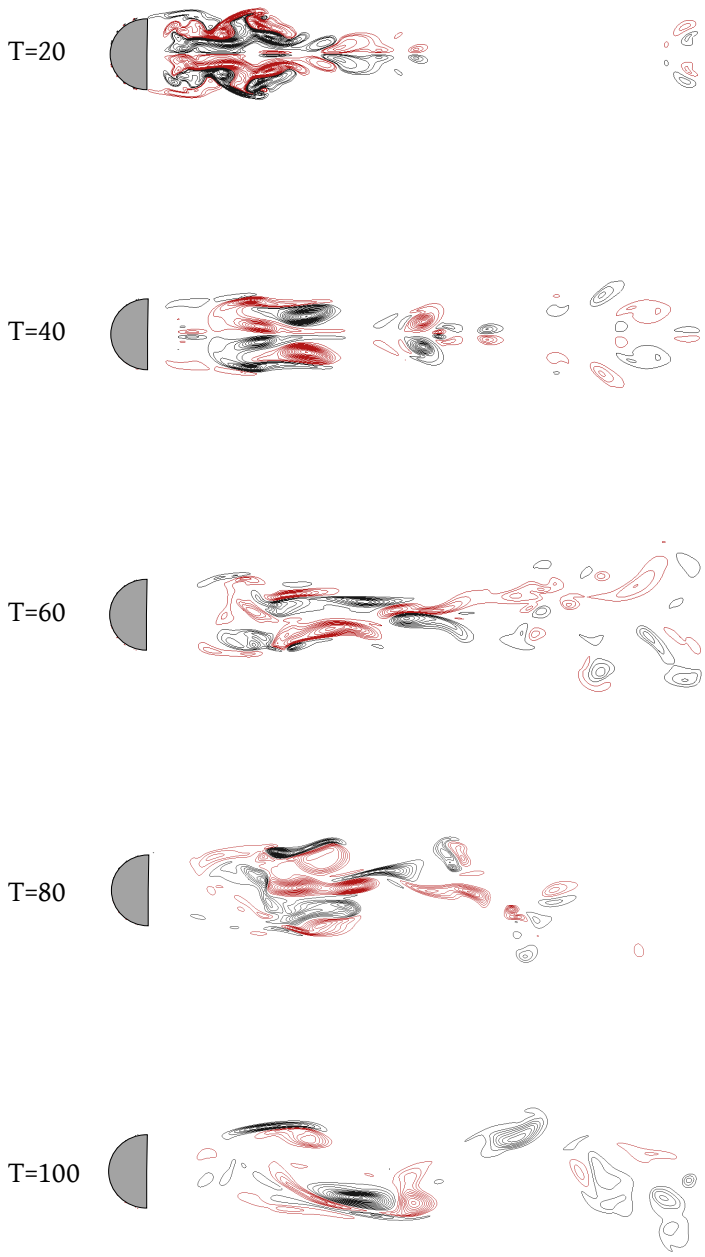

Figure 18: Isocontours of ω_x in the XZ plane for flow past a hemisphere at $Re = 1000$.

	Sphere $Re = 300$	Hemisphere $Re = 300$	Sphere $Re = 1000$	Hemisphere $Re = 1000$
Resolution	512×256^2 ($\sim$ 33M pts)	512×256^2 ($\sim$ 33M pts)	1024×512^2 ($\sim$ 268M pts)	1024×512^2 ($\sim$ 268M pts)
t_{end}	75	450	57	112
N time steps	6844	42590	11397	22352
Δt_{adapt} (mean)	$1.1\ 10^{-2}$	$1.0\ 10^{-2}$	$5.0\ 10^{-3}$	$5.0\ 10^{-3}$
N cores	32	32	64	64
CPU time	16 hours	4 days	5 days	10 days

Table 5: Parameter settings and CPU time costs for simulations of incompressible flows past a 3D sphere and hemisphere at $Re = 300$ and $Re = 1000$.

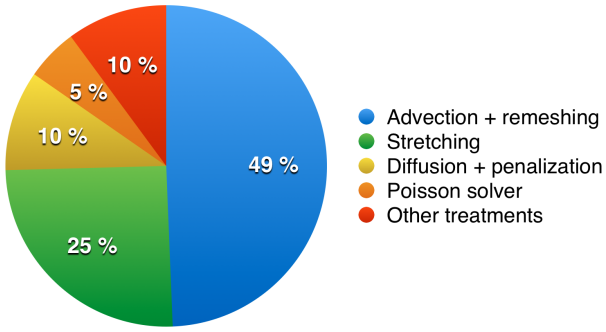

Figure 19: Percentage of the different stages implied in the resolution of the 3D penalized Vorticity-Transport-Equations (3)-(4), in one simulation time step for the execution on 1 core.

sible to rely on simple and efficient FFT based Poisson solvers for the evaluation of the velocity. Another original feature presented in this work concerns the remeshing process. The particle redistribution is indeed performed direction by direction, which allows significant computational savings in 3D compared to classical tensorial approaches.

The validation studies reported in the second part of this paper were first carried out in the case of flow past a 3D sphere. Grid-refinement studies enabled us to identify a global 2^{nd} order of convergence for the method. Careful comparisons with several numerical and experimental reference works in the literature showed satisfactory agreements. Similar studies were then performed considering a 3D hemisphere. Validations were supplied for Reynolds numbers between 200 and 300. The simulation of flow past a hemisphere

at $Re = 1000$ was finally performed. The numerical results reported in this work prove the ability of the present method to correctly account for the expected behavior of the flow at transitional or highly transitional regimes and to accurately handle geometries showing sharp edges. A study of the computational cost of the method and of its scalability on parallel computers confirms that the method provides a versatile tool to analyze bluff-body flows.

However, when increasing the Reynolds number it can easily be foreseen that using uniform Cartesian grid would quickly require prohibitive mesh sizes in order to correctly capture the thin boundary layer in DNS. Domain decomposition techniques and/or adaptive particle methods, in the spirit of [42, 32, 43], are appealing extensions of remeshed particle methods which will become mandatory in these regimes. The challenge will then be to reach a high degree of adaptivity while keeping the simplicity and associated good scalability of the penalized remeshed particle methods. Another, complementarity direction that we plan to investigate is the implementation in the context of vortex methods of second order penalization methods [44].

References

[1] G.-H. Cottet, P. Koumoutsakos, Vortex Methods - Theory and Practice, Cambridge University Press, 2000.

[2] L. Greengard, V. Rokhlin, A fast algorithm for particle simulations, J. Comput. Phys. 73(2) (1987) 325–348.

[3] P. Koumoutsakos, A. Leonard, High-resolution simulations of the flow around an impulsively started cylinder using vortex methods, J. Fluid Mech. 296 (1995) 1–38.

[4] P. Ploumhans, G. S. Winckelmans, J. K. Salmon, A. Leonard, M. S. Warren, Vortex methods for direct numerical simulation of three-dimensional bluff body flows: Applications to the sphere at $Re = 300$, 500 and 1000, J. Comput. Phys. 178 (2002) 427–463.

[5] Y. M. Marzouk, A. F. Ghoniem, K-means clustering for optimal partitioning and dynamic load balancing of parallel hierarchical N-body simulations, J. Comput. Phys. 207(2) (2005) 493–528.

[6] D. Rossinelli, Multiresolution flow simulations on multi/many-core architectures, Ph.D. thesis, ETH Zurich (2011).

[7] R. Yokota, L. A. Barba, FMM-based vortex method for simulation of isotropic turbulence on GPUs compared with a spectral method, Computers and Fluids 80 (2013) 17–27.

[8] M. Ould-Salihi, G.-H. Cottet, M. El Hamraoui, Blending finite-difference and vortex methods for incompressible flow computations, SIAM J. Sci. Comp. 22 (2000) 1655–1674.

[9] G.-H. Cottet, P. Poncet, Advances in direct numerical simulation of 3D wall-bounded flows by Vortex-In-Cell methods, J. Comput. Phys. 193 (2003) 136–158.

[10] G.-H. Cottet, J.-M. Etancelin, F. Perignon, C. Picard, High order semi-lagrangian particles for transport equations: numerical analysis and implementation issues, ESAIM: Mathematical Modelling and Numerical Analysis 48 (2014) 1029–1060.

[11] B. Schrader, I. Sbalzarini, S. Redoux, Discretization correction of general integral PSE operators for particle methods, J. Comput. Phys. 229 (2010) 4159–4182.

[12] E. Rossi, A. Colagrossi, B. Bouscasse, G. Graziani, The diffused vortex hydrodynamics method, Commun. Comput. Phys. 18(2) (2015) 351–379.

[13] E. Rossi, A. Colagrossi, D. Durante, G. Graziani, Simulating 2D viscous flow around geometries with vertices through the Diffused Vortex Hydrodynamics method, Comput. Methods Appl. Mech. Engrg. 302 (2016) 147–169.

[14] P. Koumoutsakos, A. Leonard, F. Pepin, Viscous boundary conditions for vortex methods, J. Comput. Phys. 113 (2014) 52–61.

[15] G. Graziani, M. Ranucci, R. Piva, From a boundary integral formulation to a vortex method for viscous flows, Computational mechanics 15 (1995) 301–314.

[16] P. Angot, C.-H. Bruneau, P. Fabrie, A penalization method to take into account obstacles in incompressible viscous flows, Numer. Math. 81 (1999) 497–520.

[17] E. Fadlun, R. Verzicco, P. Orlandi, J. Mohd-Yusof, Combined immersed-boundary finite-difference methods for three-dimensional complex flow simulations, J. Comput. Phys. 161(1) (2000) 35–60.

[18] N. Kevlahan, J. M. Ghidaglia, Computation of turbulent flow past an array of cylinders using a spectral method with Brinkman penalization, Eur. J. Mech. B 20 (2001) 333–350.

[19] M. Coquerelle, G.-H. Cottet, A vortex level-set method for the two-way coupling of an incompressible fluid with colliding rigid bodies, J. Comput. Phys. 227 (2008) 9121–9137.

[20] M. Gazzola, P. Chatelain, W. M. van Rees, P. Koumoutsakos, Simulations of single and multiple swimmers with non-divergence free deforming geometries, J. Comput. Phys. 230 (2011) 7093–7114.

[21] D. Rossinelli, M. Bergdorf, G.-H. Cottet, P. Koumoutsakos, GPU accelerated simulations of bluff body flows using vortex particle methods, J. Comput. Phys. 229 (2010) 3316–3333.

[22] C. Mimeau, I. Mortazavi, G.-H. Cottet, Passive Flow Control Around a Semi-Circular Cylinder Using Porous Coatings., International Journal of Flow Control 6 (2014) 43–60.

[23] C. Mimeau, F. Gallizio, G.-H. Cottet, I. Mortazavi, Vortex penalization method for bluff body flows, Int. J. Numer. Meth. Fluids 79 (2015) 55–83.

[24] A. Magni, G.-H. Cottet, Accurate, non-oscillatory remeshing schemes for particle methods, J. Comput. Phys. 231(1) (2012) 152–172.

[25] J. P. Caltagirone, Sur l'intéraction fluide-milieu poreux : Application au calcul des efforts exercés sur un obstacle par un fluide visqueux, C. R. Acad. Sci. Paris 318 (1994).

[26] D. A. Nield, A. Bejan, Convection in Porous Media, Springer, 1999.

[27] F. Morency, H. Beaugendre, F. Gallizio, Aerodynamic force evaluation for ice shedding phenomenon using vortex in cell scheme, penalisation and level set approaches, International Journal of Computational Fluid Dynamics 26(9–10) (2012) 435–450.

[28] F. Noca, D. Shiels, D. Jeon, A comparison of methods for evaluating time-dependent fluid dynamic forces on bodies, using only velocity fields and their derivatives, J. Fluids Struct. 13 (1999) 551–578.

[29] S. J. Parker, S. Balachandar, Stability and vortex shedding of bluff body arrays, Tech. rep., Air Conditioning and Refrigeration Center. College of Engineering. University of Illinois at Urbana-Champaign. (2001).

[30] A. J. Chorin, Numerical study of slighly viscous flow, J. Fluid Mech. 57 (1973) 785–796.

[31] S. Gottlieb, C. W. Shu, Total variation diminishing Runge-Kutta schemes, Mathematics of Computation 67 (1998) 73–85.

[32] M. Bergdorf, P. Koumoutsakos, A Lagrangian particle-wavelet method, SIAM Multiscale Model. Simul. 5 (2006) 980–995.

[33] T. A. Johnson, V. C. Patel, Flow past a sphere up to a Reynolds number of 300, J. Fluid Mech. 378 (1999) 19–70.

[34] F. W. Roos, W. W. Willmarth, Some experimental results on sphere and disk drag, AIAA J. 9 (1971) 285–291.

[35] A. Tomboulides, A. Orszag, Numerical investigation of transitional and weak turbulent flow past a sphere, J. Fluid Mech. 416 (2000) 45–73.

[36] G. S. Constantinescu, K. D. Squires, LES and DES investigations of turbulent flow over a sphere., AIAA Paper 2000-0540 (2000).

[37] D. Kim, H. Choi, Laminar flow past a sphere rotating in the streamwise direction, J. Fluid Mech. 461 (2002) 365–386.

[38] J. Wu, G. Faeth, Sphere wakes in still surroundings at intermediate Reynolds numbers, AIAA J. 31(8) (1993) 1448–1455.

[39] E. Poon, G. Iaccarino, A. Ooi, M. Giacobello, Numerical studies of high Reynolds number flow past a stationary and rotating sphere, Seventh International Conference on CFD in the Minerals and Process Industries CSIRO, Melbourne, Australia (2009).

[40] R. Campregher, J. Militzer, S. Mansur, A. da Silveira Neto, Computations of the flow past a still sphere at moderate Reynolds numbers using an immersed boundary method, J. of the Braz. Soc. of Mech. Sci. & Eng. 31(4) (2009) 344–352.

[41] D. Kim, H. Choi, Laminar flow past a hemisphere, Physics of Fluids 15(8) (2003) 2457–2460.

[42] M. Bergdorf, G.-H. Cottet, P. Koumoutsakos, Multilevel adaptive particle methods for convection-diffusion equations, Multiscale Modeling and Simulation: A SIAM Interdisciplinary Journal 4(1) (2005) 328–357.

[43] D. Rossinelli, B. Hejazialhosseini, W. M. van Rees, M. Gazzola, M. Bergdorf, P. Koumoutsakos, MRAG-I2D: Multi-resolution adapted grids for remeshed vortex methods on multicore architectures, J. Comput. Phys. 288 (2015) 1–18.

[44] M. Bergmann, J. Hovnanian, A. Iollo, An accurate cartesian method for incompressible flows with moving boundaries, Commun. Comput. Phys. 15(5) (2014) 1266–1290.